EES Catalysis

PAPER

View Article Online
View Journal

Cite this: DOI: 10.1039/d6ey00019c

Corrosion-resistant mesoporous carbon allowing for durable, high-performance hydrogen fuel cells for heavy-duty vehicle applications

Marwa Atwa, *[a] Sara Pedram,[b] Shicheng Xu,[ac] Samuel Dull,[d] Yunha Jung,[e] Takeharu Yoshii,[f] Ruohong Sui,[g] Rong Xu,[e] Robert Marriott,[g] Hirotomo Nishihara,[f] Jonathan E. Mueller,[h] Marco Wiethop,[h] Sebastian Kirsch,[h] Gerold Huebner,[h] Vedran Glavas,[hi] Jasna Jankovic,[b] Thomas F. Jaramillo *[dj] and Fritz B. Prinz*[acjk]

Proton exchange membrane fuel cells (PEMFCs) have emerged as an efficient and clean energy conversion technology, utilizing platinum (Pt)-based catalysts to drive the electrochemical reactions that generate power, including nanoporous carbon-supported Pt nanoparticles. However, developing catalyst layers with exceptional stability has been a challenge, which is essential to achieving the 25 000-hour lifetime required for heavy-duty fuel cell applications. While Pt stability is critical, mitigating carbon support corrosion in the catalyst layer is equally important. Here, we show that tuning the properties of mesoporous carbon supports—specifically, pore size and the concentration of surface oxygen functional groups and H-terminated groups *via* high-temperature treatment—can overcome this challenge. Pore sizes of 8 nm or smaller are found to mitigate Pt dissolution and performance losses over 10 000–90 000 accelerated stress cycles. Additionally, high-temperature treatment at 2000 °C increased the carbon's crystallinity while retaining a BET surface area of 240 $m^2\ g^{-1}$. This stability enabled the catalyst layer to maintain its initial performance after 40 hours of voltage hold at 1.2 V, demonstrating exceptional durability. These advancements are a critical step toward commercializing fuel cells for transportation applications and provide insights for advanced catalyst layer designs in clean energy conversion systems.

Received 24th January 2026,
Accepted 2nd February 2026

DOI: 10.1039/d6ey00019c

rsc.li/eescatalysis

Broader context

Proton exchange membrane fuel cells (PEMFCs) are among the most promising clean energy technologies, offering high efficiency and zero emissions through platinum (Pt)-based catalysts that drive hydrogen and oxygen conversion into electricity. However, achieving the durability needed for heavy-duty applications—up to 25 000 hours—remains a challenge due to catalyst degradation and carbon support corrosion. Tailoring mesoporous carbon supports by controlling pore size and crystallinity enhances durability, suppressing Pt nanoparticle dissolution and aggregation. Mesoporous carbons with sub-8 nm pores and high-temperature graphitization at 2000 °C maintain high surface area (240 $m^2\ g^{-1}$) and resist oxidative corrosion, retaining catalytic activity after extensive durability tests. These corrosion-resistant, porous graphitic carbons are also ideal for water electrolyzers, CO_2/CO electrolysis, and supercapacitors, serving as stable supports under harsh conditions. Advances in meso- and graphitic-carbon architectures thus offer a unifying strategy for scalable, long-lifetime electrochemical energy conversion and storage systems.

---

[a] *Department of Mechanical Engineering, Stanford University, Stanford, CA 94305, USA. E-mail: marwaatw@stanford.edu, fprinz@stanford.edu*
[b] *Department of Materials Science and Engineering, University of Connecticut, Storrs, CT 06269, USA*
[c] *Jinetics Inc., 297 Bernardo Ave, Mountain View, CA, 94043, USA*
[d] *Department of Chemical Engineering, Stanford University, Stanford, CA, 94305, USA. E-mail: jaramillo@stanford.edu*
[e] *Department of Materials Science and Engineering, Stanford University, Stanford, CA, 94305, USA*
[f] *Advanced Institute for Materials Research (WPI-AIMR)/Institute of Multidisciplinary Research for Advanced Materials, Tohoku University, Sendai, 980-8577, Japan*
[g] *Department of Chemistry, University of Calgary, 2500 University Dr NW, Calgary, AB, T2N 1N4, Canada*
[h] *Volkswagen AG, Berliner Ring 2, 38440 Wolfsburg, Germany*
[i] *Department of Mechanical Engineering, Mannheim Technical University of Applied, Mannheim, 68163, Germany*
[j] *SUNCAT Center for Interface Science and Catalysis, SLAC National Accelerator Laboratory, Menlo Park, CA 94025, USA*
[k] *Department of Mechanical and Industrial Engineering, Norwegian University of Science and Technology, Trondheim, 7491, Norway*

Introduction

Proton exchange membrane fuel cells (PEMFCs) have emerged as a promising technology for heavy-duty vehicle applications, offering a clean, efficient alternative to traditional fossil-fuel-powered engines.[1] As the transportation sector seeks to reduce its carbon footprint, PEMFCs have attracted significant attention for their high power density, low operating temperature, and potential for zero-emission operation.[2]

The transition from light-duty to heavy-duty vehicle applications has shifted the focus of PEMFC research and development. While initial concerns centered on reducing capital costs, the emphasis has shifted towards improving durability and lowering operating costs over the lifetime of the fuel cell system.[3,4]

Different components of a single PEM fuel cell device can undergo various types of degradation, significantly impacting performance and longevity. Recent studies have provided valuable insights into these processes.[5] For instance, the polymer electrolyte membrane (PEM), typically made of Nafion, can undergo chemical and mechanical degradation, leading to thinning and pinhole formation.[6] Gas diffusion layers may experience changes in hydrophobicity and structure, affecting water management and gas transport.[5,7] The catalyst layer, particularly on the cathode side, undergoes substantial degradation over the lifetime of a cell, with platinum nanoparticles experiencing dissolution, agglomeration, and detachment, leading to a reduction in the electrochemically active surface area.[8–10] The carbon support in the catalyst layer may also corrode, especially under high potential conditions.[11,12] Among these degradation pathways, catalyst layer stability, including catalyst and carbon support, remains one of the largest contributors that limits the longevity of PEMFCs.

Catalyst dissolution, particularly of platinum (Pt) and its alloys, remains a significant challenge in PEMFCs. Several mitigation strategies have been developed to address this issue. One approach involves alloying Pt with other transition metals like cobalt, nickel, or iron to enhance stability.[13,14] Another method is the use of core–shell nanostructures, where a more stable metal core is coated with a thin Pt shell, reducing overall Pt content while maintaining catalytic activity.[15,16] Surface modification techniques, such as the addition of atomic layers of stable metals or metal oxides, have also shown promise in improving durability.[17–19] However, these methods often face limitations in long-term stability, especially under dynamic operating conditions. Some alloying elements may leach out over time, and core–shell structures can degrade in harsh electrochemical environments. Furthermore, the trade-off between enhancing stability and maintaining high catalytic activity remains a significant challenge in developing truly durable PEMFC catalysts.

In a recent study, Liu and co-workers[20] designed a graphene-nanopocket-protected, pore-confined, Pt nanocatalyst supported on Ketjenblack carbon (KB), which was tested for heavy-duty fuel cell applications. The catalyst showed minimal performance loss of only 1.1% after 90 000 cycles of accelerated stress testing (AST), consisting of square-wave cycles between 0.6 V and 0.95 V with 3-second holds at each potential, which specifically probe for Pt dissolution. However, durability testing for carbon corrosion was not performed in this study.

While Pt dissolution dominates early degradation, carbon support corrosion becomes the limiting factor in long-term durability - a single start-up/shutdown event at 1.5 V can cause more carbon loss than 30 000 cycles below 1 V.[12,21] The collapse of the catalyst layer architecture ultimately determines cell lifespan, making carbon corrosion mitigation equally critical to Pt stabilization. Therefore, researchers have developed several strategies to mitigate the corrosion of carbon supports of PEMFC cathodes. These include surface modification of carbon supports through graphitization and nitrogen doping, using alternative carbon structures like carbon nanotubes and graphene-based supports, and developing hybrid supports combining carbon with metal oxides or conductive polymers.[22–24] However, there are often trade-offs between corrosion resistance and other aspects of fuel cell performance, such as catalytic activity or mass transport properties.[25] Combining both catalyst and carbon stability in one PEMFC cathode without compromising performance and durability has not been achieved yet.

In the current study, atomic layer deposition (ALD) was used to deposit Pt onto a mesoporous carbon support. While prior studies—including our own—have applied ALD to porous carbon materials and composites to optimize Pt loading and nanoparticle size by controlling ALD cycle numbers, these works typically address only one or two of the three interrelated challenges in PEMFC catalyst layers: activity, performance, and stability.[26–30] Furthermore, discussions of stability in the literature primarily focus on mitigating Pt dissolution, while carbon corrosion is often neglected.

In contrast, the present study demonstrates a cathode catalyst layer that simultaneously achieves high performance, high activity, and enhanced stability by addressing both Pt dissolution and carbon corrosion. This is accomplished by integrating Pt with highly graphitized, highly porous mesoporous carbon supports, enabling durable operation under demanding heavy-duty conditions.

In this work, we optimize a mesoporous carbon, including its surface properties, including pore size and crystallinity, to serve as a durable carbon support in a PEMFC cathode that meets and exceeds the activity, performance, and stability requirements (both catalyst dissolution and carbon corrosion) for heavy-duty applications. This represents a rare combination of these critical characteristics in a single catalyst layer electrode setup. The durability metrics of these cathodes meet the requirements of hydrogen fuel cells for heavy-duty vehicles, *i.e.* >1.07 A cm^{-2} at 0.7 V after 90 000 cycles of AST for Pt dissolution and performance retention after 40 hours of potential hold at 1.2 V as AST for carbon corrosion.

Results and discussions

Physical and surface properties of mesoporous carbon powders (MCP)

Two mesoporous carbon powders (MCP) were prepared using a modified hard template method with silica nanoparticles of 8 and 12 nm average size. The resulting two mesoporous carbon powders (MCP), MCP8 and MCP12, with nominal pore sizes of 8 and 12 nm, were further characterized using a wide scope of techniques (details are found in the Experimental section).

Nitrogen gas sorption analysis was used to analyze porous structure, including pore size distribution, pore volume, and extraction of the Brunauer–Emmett–Teller (BET) surface area.[31] Fig. 1a shows the nitrogen adsorption and desorption isotherms of MCP8 and MCP12. According to IUPAC classifications, the isotherms for MCP8 and MCP12 powders are Type IV with H2 hysteresis, indicating uniform pore sizes and strong pore interconnectivity. These results also suggest that narrow pore necks and limited cross-sectional surface areas constrain N_2 gas adsorption and desorption within the MCP porous structure.[32] To reveal the pore and pore neck size distribution, the Barrett, Joyner, and Halenda (BJH) method[33] was used for both MCP8 and MCP12, as shown in Fig. 1b. Both MCP8 and MCP12 have similar pore neck sizes of ∼ 4.6 nm, with an average pore size of 6.4 nm and 8.8 nm, respectively. The pore size of MCP12 is 1.3 times larger than that of MCP8, with MCP12 having a broader pore size distribution (2–15 nm) than MCP8 (2–8 nm). The specific surface area (S_{BET}) of the MCPs was extracted from the nitrogen isotherm using the BET method (Table S1). The micropore surface area (S_{micro}) was calculated using the *t*-plot method reported by Lippens and De Boer.[34] The total pore volume was estimated at a relative pressure of 0.98. The specific surface area and total pore volume (V_{NSI}) of the MCP12 are lower than those of the MCP8, which is attributed to the increase in pore size, as shown in Table S1. Based on previous studies, differences in pore size and pore volume between MCP8 and MCP12 could potentially affect both the mass activity and stability of the Pt/MCP catalyst layer (CL).[29,30,35–37]

For further investigation of the microstructure, including surface chemistry, X-ray photoelectron spectroscopy (XPS) and high-resolution transmission electron microscopy (HR-TEM) were used. No significant differences have been observed in the surface carbon species and morphology of MCP8 and MCP12, as shown in Fig. 1c and d, respectively. The C 1s XPS spectra for MCP8 and MCP12 revealed the coexistence of hydrogen-terminated, hydroxide, carbonyl, and acetate surface functional groups (Fig. 1c). HR-TEM images also showed ordered, porous, spherical structures for MCP8 and MCP12, consistent with the silica templates used to prepare these mesoporous carbon powders (Fig. 1d).

Fabrication of Pt/MCP gas diffusion electrodes

The electrodes tested here, as gas diffusion electrodes (GDEs), were fabricated using the bottom-up electrode fabrication method previously reported by our group.[38] Fig. 2a shows our GDE fabrication process, in which a 2–5 μm layer of carbon is deposited onto the microporous layer of a gas diffusion layer *via* ultrasonic spraying. Pt is then grown on the carbon using 20–30 cycles of atomic layer deposition (ALD), depending on the targeted mass loading of Pt. It is worth noting that the Pt nanoparticle distribution is similar across the thickness of the Pt/MCP catalyst layer (only 0.5 nm difference), as evidenced by TEM analysis. Representative TEM images taken from the

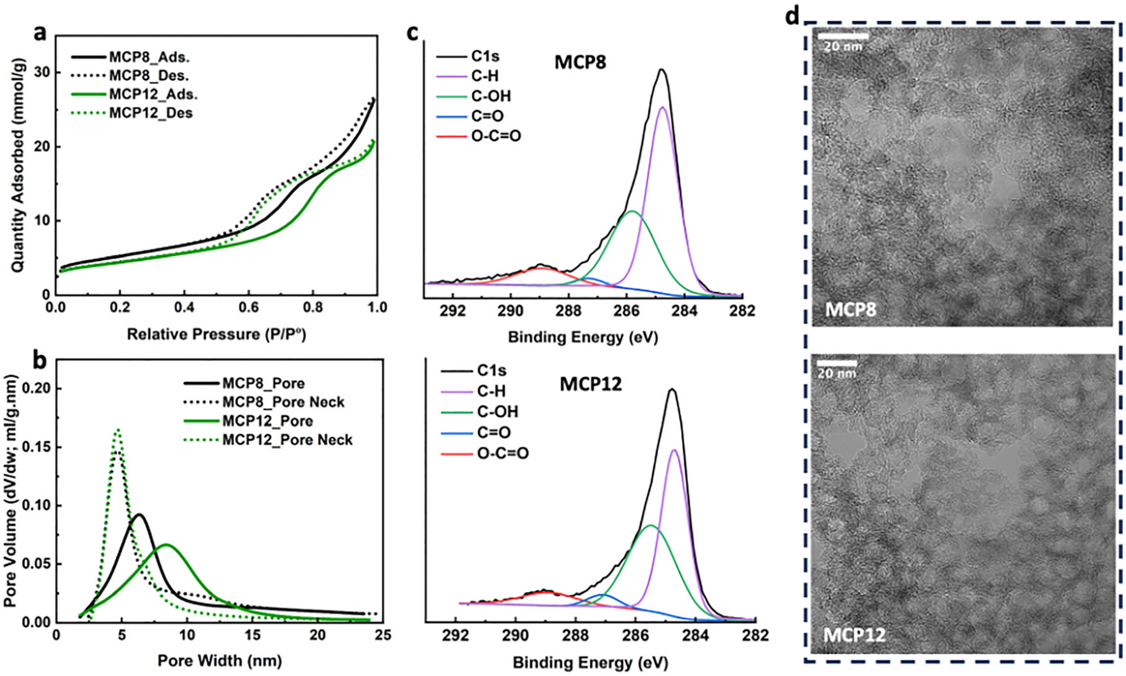

Fig. 1 Morphological, pore, and surface characteristics of mesoporous carbon powders with nominal pore sizes of 8 nm (MCP8) and 12 nm (MCP12). (a) Nitrogen gas sorption analysis of MCP8 and MCP12. (b) Pore size distribution (PSD) of MCPs obtained from the N_2 gas sorption isotherm (BJH method), with the adsorption branch (solid lines), giving the average pore diameter, and the desorption branch (dotted lines), giving the average pore neck size. (c) High-resolution X-ray photoelectron spectra of MCP8 (top) and MCP12 (bottom) at the C 1s binding energy and their fitted curves. (d) High-resolution transmission electron micrograph (HR-TEM) of MCP8 and MCP12.

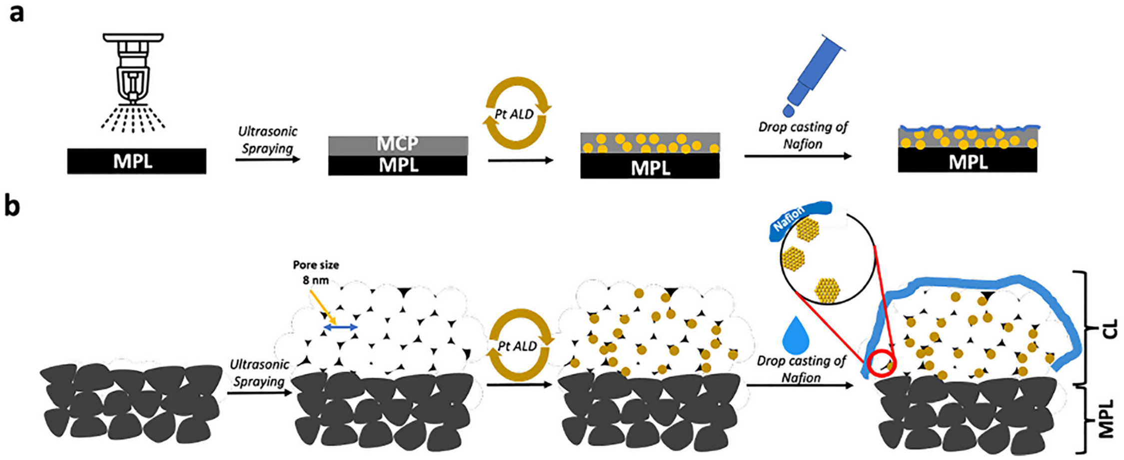

Fig. 2 Schematic illustration of the fabrication method of gas diffusion electrodes (GDEs) of mesoporous carbon powder (MCP). (a) Schematic showing Pt/MCP catalyst layer coatings on the microporous layer (MPL) starting with ultrasonic carbon spraying, then atomic layer deposition (ALD) of Pt, and finally drop-casting of Nafion solution. (b) Illustration of the microstructure of the catalyst layer (CL) at each step of fabrication: carbon spraying, Pt ALD, and Nafion impregnation.

surface of the catalyst layer (facing the membrane), the middle of the layer, and the interface between the catalyst layer and the MPL for Pt/MCP8 are shown in Fig. S1 and S2. As the last step in the fabrication process, the catalyst layer is impregnated with ionomer by drop-casting a dilute ionomer (0.5 wt%) dispersion onto the surface of the Pt/carbon layer with a target ionomer/carbon (I/C) ratio of 4. It is worth noting that this fabrication method enabled the formation of a thin layer of Pt/carbon powder without adding Nafion to the sprayed ink. Thus, the first two steps in the fabrication process were performed in the absence of ionomer. Fig. 2b illustrates a schematic representation of the microstructure formed during the GDE fabrication process. It is worth noting that Nafion was distributed mainly outside the pores and the carbon agglomerate, as seen in the energy-dispersive X-ray spectroscopy (EDS) maps of fluorine in the TEM images in Fig. S3–S6. Cross-sectional scanning transmission electron microscopy (STEM)-EDS images and elemental EDS maps of Pt/MCP8 (Fig. S3) confirm the homogenous distribution of Pt NPs throughout the carbon layer.

Electrochemical testing in MEA in a Single PEMFC

Performance and activity. For testing, Pt/MCP-based GDEs were assembled with commercial 0.1 mg_{Pt} cm^{-2} anode-coated membranes. The ALD-prepared GDEs were conditioned and tested for ORR activity under differential flow at 80 °C, 100% relative humidity (RH), and 50 kPa backpressure (150 kPa absolute back pressure). It is worth noting that during conditioning, the Nafion distribution undergoes significant morphological changes that enhance proton transport pathways during cell operation.[39] The conditioning process establishes more proton transport pathways, promotes more uniform membrane hydration, and activates additional reaction sites.[39] These structural modifications result in improved ionomer coverage and enhanced proton conductivity due to the swelling properties of the ionomer under hydrated conditions.[40,41]

We also compared electrochemical results for Pt/MCP-based GDEs with those of the commercial KB nanoporous carbon, which was sprayed onto MPL/GDL and used as a substrate for Pt ALD (prepared using the same procedure as for the Pt-MCP samples). Three sets of samples were tested: Pt/MCP8, Pt/MCP12, and Pt/KB GDEs. All three electrodes have the same Pt mass loading (0.1 mg_{Pt} cm^{-2}) and an I/C ratio of 4.

Fig. 3a shows that Pt/MCP8 and Pt/MCP12 have higher mass activities compared to Pt/KB. The high mass activity of Pt/MCP GDEs (*ca.* 0.5 A mg_{Pt}^{-1}), which is almost twice the mass activity of Pt/KB (*ca.* 0.3 A mg_{Pt}^{-1}), can be attributed to the screening effect of ionomer poisoning as MCP pore size is big enough to host Pt NPs inside, but small enough to prevent infiltrate ionomer leaving it mostly outside the pores (Fig. 3a).[35] For reference, most of the pores in KB are micropores, which are less than 2 nm in diameter (according to IUPAC, pores with <2 nm are micropores).[32,42] Due to the microporous nature of KB, Pt grows outside the primary pores, and is therefore poisoned by Nafion, leading to a loss in activity and performance compared to Pt/MCP-based GDEs.

The confinement of ionomer to the surface of the Pt/MCP agglomerates has been confirmed by the EDS mapping of the cross-section of the electrodes (represented by the Fluorine EDS map) in Fig. S3–S5. Almost no ionomer exists inside the agglomerate, where most Pt nanoparticles are located. This confirms that the MCP8 porous structure allows for the uniform distribution of Pt nanoparticles inside and outside the carbon agglomerates while allowing Nafion to infiltrate only on the outside surface of the carbon agglomerate. The same Pt and Nafion distribution is observed in the Pt/MCP12 GDE. Thus, the performance and activity of Pt/MCP12 is expected to be similar to that of Pt/MCP8.

The electrochemical active surface area (ECSA) was obtained from the hydrogen under potential deposition (HUPD) in the cyclic voltammetry in H_2/Ar at 80 °C for all three GDEs. Based on the cyclic voltammograms collected and shown in Fig. 3b,

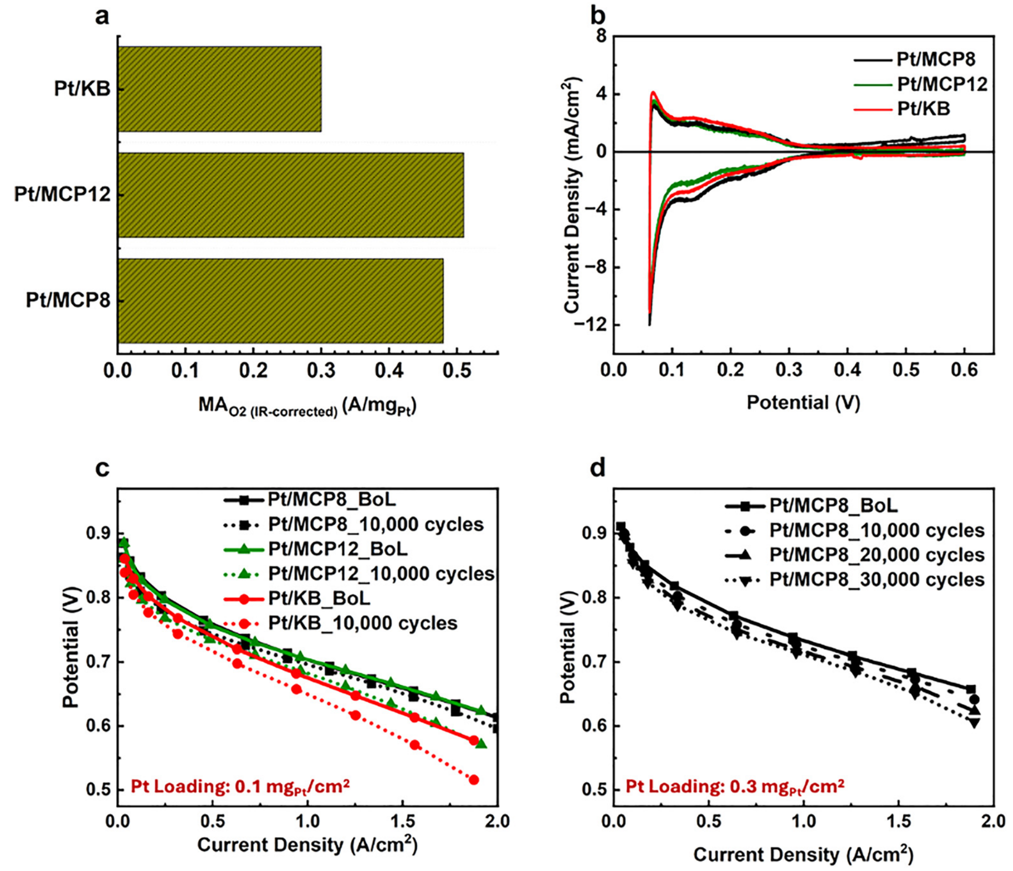

Fig. 3 Electrochemical performance of Pt/MCP8, Pt/MCP12 catalyst layers and state-of-the-art commercial Pt/C powder catalyst layer (Pt/KB) in PEMFC MEAs. (a) IR-corrected H_2/O_2 mass activities at 100% RH, 150 kPa_{abs}, and 80 °C. Pt mass loading in these three types of GDE is 0.1 mg_{Pt} cm^{-2}. (b) CVs (20 mV s^{-1}, humidified H_2/Ar, 100% RH values. (c) H_2/Air performance (non IR-corrected) of MEAs of Pt/KB, Pt/MCP8, and Pt/MCP12 (Pt mass loading in all samples = 0.1 mg_{Pt} cm^{-2}) at BoL and EoL (after 10 000 AST square-wave cycles between 0.6 V and 0.95 V in 100% RH, with 3 second holds at each potential) at 100% RH, 150 kPa_{abs}, and 80 °C. (d) H_2/Air performance (non IR-corrected) of MEAs of Pt/MCP8 (Pt mass loading = 0.3 mg_{Pt} cm^{-2}) at BoL and EoL (after 30 000 AST square-wave cycles between 0.6 V and 0.95 V in 100% RH, with 3 second holds at each potential) at 100% RH, 150 kPa_{abs}, and 80 °C.

Pt/KB has the highest ECSA value (64.7 m^2 g_{Pt}^{-1}) compared with Pt/MCP12 (38.8 m^2 g_{Pt}^{-1}) and Pt/MCP8 (49.1 m^2 g_{Pt}^{-1}). Furthermore, both Pt/MCP8 and Pt/MCP12 showed similar beginning-of-life (BoL) performance and activity that is significantly higher than Pt/KB (Fig. 3a and c). Based on our previous studies, mesoporous carbon materials allow uniform Pt deposition *via* ALD.[29,30] However, pore size would be small enough not to allow Nafion to penetrate the pores, preventing the poisoning of Pt nanoparticles.

Pt dissolution. We studied the stability of active and durable Pt/MCP8 and Pt/MCP12 electrodes for Pt dissolution by performing 10 000 voltage cycles of accelerated stress test (AST; voltage cycling between 0.6 V and 0.9 V, with holds of 3 s at each voltage) compared to Pt/KB. The results in Fig. 3c reveal the high stability of the Pt/MCP8 catalyst layer, where the performance is almost fully retained after 10 000 cycles (with no current density decrease at 0.7 V). In comparison, a loss of 20% and 22% in the performance of Pt/KB and Pt/MCP12, respectively, has been observed in Fig. 3c.

Furthermore, we conducted over 30 000 cycles with Pt/MCP8, featuring a higher Pt mass loading (0.3 mg_{Pt} cm^{-2}), to evaluate its suitability for heavy-duty applications. The results, shown in Fig. 3d, revealed performance losses after 30 000 cycles of Pt dissolution. The electrochemically active surface area of this sample remained unchanged up to 10 000 cycles, followed by a 34% decrease after 20 000 cycles and an additional 8% decrease after 30 000 cycles, amounting to a total 42% reduction in ECSA. This suggests that the most significant changes occurred after 20 000 cycles. Nevertheless, the reduction in ECSA does not necessarily translate into performance losses, a finding consistent with previous studies.[37]

The origin of mitigation of Pt dissolution. We investigated the Pt/MCP GDEs after Pt dissolution. First, TEM and EDS analyses were conducted (see Fig. S6 and S7), revealing Pt agglomerates on the outer surface of the carbon particles. To further examine the Pt size distribution after Pt dissolution, we performed *ex situ* TEM analysis on cross-sections of Pt/MCP8 and Pt/MCP12 MEAs (with 0.1 mgPt cm^{-2} loading; stability and performance shown in Fig. 3c), as presented in Fig. 4. We investigated the size distribution of Pt nanoparticles on the inner and outer surfaces of a carbon agglomerate (*i.e.*, within the secondary porosity) at both the beginning of life

(BoL) and end of life (EoL). As mentioned earlier, Pt nanoparticles likely reside within the 8–12 nm pores that constitute the primary porosity. However, Pt nanoparticle agglomeration is more prominent in the secondary porosity, where larger void spaces facilitate Pt nanoparticle coalescence *via* Ostwald ripening. Notably, the observed agglomeration behavior reflects the influence of the primary pores and their confinement effect in inhibiting nanoparticle coalescence and mitigating Pt dissolution and associated performance losses. The spatial distribution of agglomerates—whether in the inner or outer regions of the carbon agglomerate—also underscores this effect. For instance, in the inner regions, the confinement imposed by primary pores is expected to limit agglomeration, whereas on the outer edges of the agglomerate, where Pt nanoparticles experience less confinement, larger agglomerates are more likely to form.

In the Pt/MCP8 MEA, a similar Pt NP size (*ca.* 1.5 nm) in both the inner and outer surfaces (Fig. 4a) was observed at BoL (Table S2). However, at the EoL (after 10 000 cycles), an observed difference in the Pt NP size between the inner and outer surface of the carbon agglomerate of the Pt/MCP8 catalyst layer (CL) is detected (Fig. 4b and Table S2). There is a significant increase in the Pt NP size of the outer surface (4.3 nm) *versus* the inner surface (2.6 nm), shown in Fig. 4c. This indicates that Pt dissolution and growth within the pores may be limited by mass transport of dissolved Pt ions through the pores and thus exhibit a strong dependence on the primary porosity. Pt NPs on the outer surface are not subject to the same transport limitations and are thus more susceptible to agglomeration and Ostwald ripening.[43] This decrease in Pt dissolution results from the pore confinement effect,[25,43] which explains the stable performance of Pt/MCP8 (Fig. 3c and d).

Moreover, we investigated the change in the Pt NP size in the MEA with the larger pore-size carbon support (MCP12). At BoL, the TEM of Pt/MCP12 presents Pt NP size (~1.5 nm) located in the inner and outer surfaces of the carbon agglomerate, similar to what has been observed in the Pt/MCP8 GDE (Fig. 4a and d). However, at EoL (after 10 000 cycles), Pt growth of both inner and outer Pt particles is more significant than in Pt/MCP8, Fig. 4e and f and Table S2, with the average inner Pt NP size of 4.8 nm, and average outer Pt NP size of 6.8 nm. This dramatic increase in the Pt NP size in Pt/MCP12 may be attributed to the presumably low mass transport resistance of dissolved Pt ions, which is likely due to the larger pore size and could explain the significant loss in the performance of Pt/MCP12 after 10 000 cycles (Fig. 3c).

Carbon corrosion in Pt/MCP8 GDEs. Despite the significant advantage of MCP8 as a carbon support in reducing Pt dissolution, it is expected to be vulnerable to carbon corrosion at high potentials (>1.0 V). This vulnerability arises from its high density of edge sites, defects, and surface functional groups. These characteristics, while beneficial for enabling a uniform distribution of Pt nanoparticles inside the pores and throughout the entire catalyst layer thickness (as observed in the current study, see Fig. S1 and S2, and previous studies on similar mesoporous carbons),[29,30] also make MCP8 more susceptible to

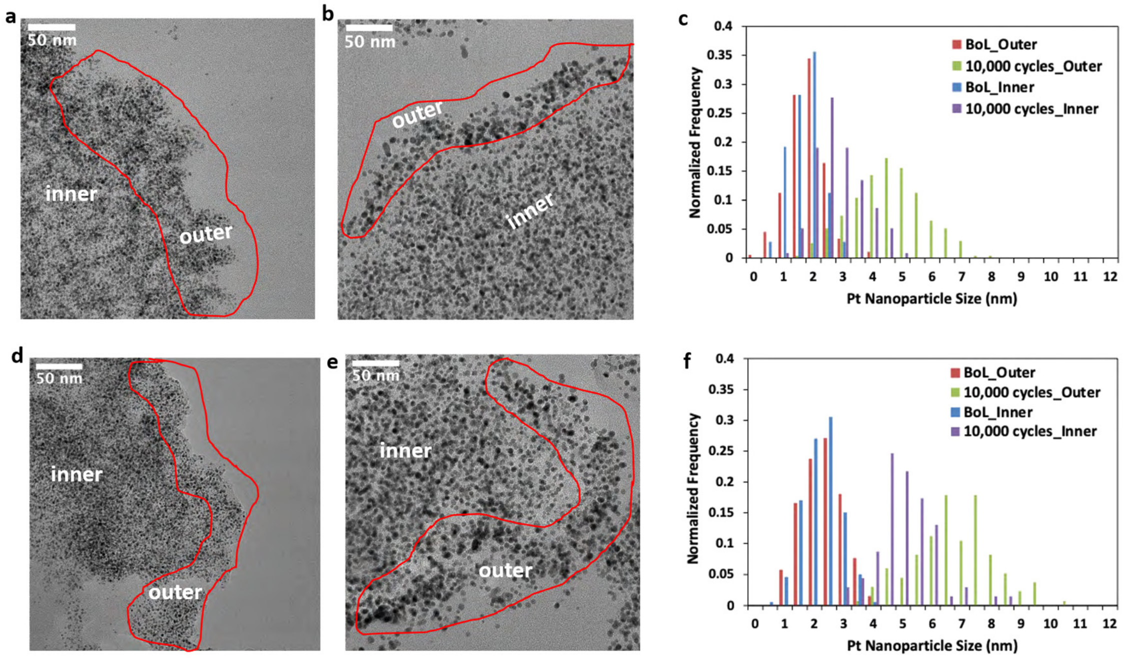

Fig. 4 TEM images with histograms of Pt nanoparticle size distribution inner (inside the pores of the carbon agglomerate; Nafion-poor area) *versus* outer (on the surface of carbon agglomerate; Nafion-rich area) for Pt/MCP catalyst layers with 0.1 mg_{Pt} cm^{-2}. (a) TEM image of Pt/MCP8 at 0 k AST cycles. (b) TEM image of Pt/MCP8 at 10 000 AST cycles. (c) A histogram shows Pt nanoparticle size distribution across the two samples (a and b). (d) TEM image of Pt/MCP12 at 0 k AST cycles. (e) TEM image of Pt/MCP12 at 10 000 AST cycles. (f) A histogram shows Pt nanoparticle size distribution across the two samples (d and e).

degradation under high-potential conditions. Thus, to enhance the resistance of MCP8 to corrosion, we heat-treated the MCP8 carbon support at 2000 °C under vacuum for 2 hours to graphitize the carbon without affecting the pore size, which is crucial for mitigating Pt dissolution. We used high resolution (HR)-TEM to visualize the changes in morphology after the heat treatment. The results in Fig. 5a and b show no morphological change in the MCP8 after the heat treatment. HR-TEM images of the heat-treated carbon (MCP8-2000) reveal more highly organized and obvious graphene layers (Fig. 5c and d), resulting from an enhancement of the graphitic structure. The higher degree of graphitization corresponds to more uniform and well-aligned lattice fringes observed in MCP8-2000 (Fig. 5d). A closer comparison of the HR-TEM images of MCP8 and MCP8-2000 carbons is shown in Fig. S8 and S9. The MCP8 sample shows a short-range order of multilayer graphene regions (Fig. S8a) with a background of amorphous carbon. At the same time, the morphology of MCP8-2000 appears to show longer-range multilayer graphene sheets (Fig. S8b).

In Fig. 5c and d, the HR-TEM images of MCP8 and MCP8-2000 and the corresponding FFT patterns reveal an interlayer spacing of 0.397 and 0.350 nm, respectively, which is larger than that of pure graphite (0.335 nm).[44] While both carbons (MCP8 and MCP-2000) show higher interlayer distance than pure graphitic carbon, MCP8-2000 shows values significantly closer to graphitic carbon. The interlayer distance of 0.350 nm in MCP8-2000 suggests the presence of structural disorder caused by defects, functionalization, or incomplete graphitization. The arrangement of disordered graphene layers and the enlarged interlayer distance indicate abundant porosity and structural versatility. These findings suggest that high-temperature treatment induces long-range graphene orientation while retaining defects that are essential for efficient Pt deposition on the carbon surface *via* ALD. Nevertheless, Fig. S10 shows the N_2 gas sorption and pore size distribution of MCP8 after the 2000 °C treatment and Table 1 presents the BET and microporous surface areas of both carbons, showing a 40% decrease in surface area after heat treatment while retaining the original pore size, which is crucial for preventing Pt dissolution.

Interestingly, the BoL performance in H_2/air of Pt/MCP8 and Pt/MCP8-2000 is similar (Fig. 5e), suggesting that the high-temperature treatment has no drastic effect on the overall performance in H_2/Air. However, it is worth noting that the BoL performance at low current density is slightly higher in Pt/MCP8 compared with Pt/MCP8-2000 and is comparable with the lower mass activity observed in pure O_2 (Fig. S11). This decrease in mass activity is due to the larger Pt NPs (3.25 ± 0.81 nm) that have been observed on MCP8-2000 compared with MCP8 (1.73 ± 0.66 nm), shown in Fig. S12. This is consistent with what has been observed in the literature when Pt is deposited on graphitic, hydrophobic, defect-free, or crystalline carbons, larger nanoparticles are observed.[45]

To investigate the effect of the high-temperature heat treatment (2000 °C) on overcoming carbon corrosion in Pt/MCP8 MEAs at high potentials, we held the potential at 1.2 V for 40 h under an H_2/Ar atmosphere (Fig. 5e). When subjected to this carbon corrosion protocol, the Pt/MCP8-2000 showed no significant performance loss, while a drastic loss in the performance of Pt/MCP8 was observed. This difference could be attributed to that the large number of defect sites in the MCP8, which are susceptible to carbon corrosion and oxidation.[46] These processes lead to oxidation to carbon dioxide or surface oxidation (forming oxygen-functional groups) of MCP8, making it more hydrophilic, leading to flooding and loss in the high current density region. In contrast, in the heat-treated, partially graphitized MCP8-2000, there a much fewer defect sites. These defects

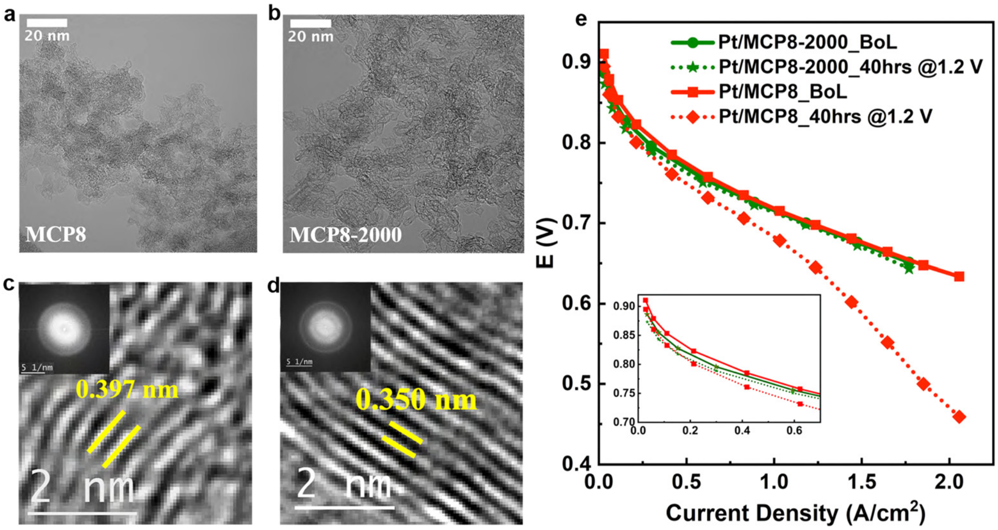

Fig. 5 Effect of high-temperature treatment (2000 °C) of MCP8 on physical properties, performance, and stability for carbon corrosion. (a and b) HR-TEM image of MCP8 and MCP8-2000 (treated at 2000 °C), respectively. (c and d) HR-TEM showing interlayer spacing on MCP8 and MCP8-2000, respectively. Inset is Fast Fourier Transform (FFT) of regions shown in c and d. (e) H_2/Air performance (non-IR-corrected) of MEAs of Pt/MCP8 and Pt/MCP8-2000 (Pt mass loading = 0.3 mgPt cm^{-2}) at BoL and EoL (after holding potential at 1.2 V for 40 h in H_2/Ar) at 100% RH, 150 kPa_{abs}, and 80 °C.

Table 1 Surface area and porous characteristics of MCP8 and MCP8-2000

Sample	BET surface area (m^2 g^{-1})	Microporous surface area (m^2 g^{-1})	Pore size (nm)	Pore neck size (nm)
MCP8	412.5	59.1	6.4	4.8
MCP8-2000	241.5	17.6	6.4	4.2

and edge sites have been reported to be the sites for corrosion.[46] These edge sites are composed of oxygen functional groups (also seen in the analysis of XPS, C 1s, Fig. 1c) and hydrogen-terminated edge sites that, when exposed to high potentials, leave the surface as a combination of CO, CO_2, H_2, and H_2O gases (Fig. S13 and Table S3). Hence, the total gas evolved during the temperature-programmed desorption (TPD) can be used as a direct quantification of oxygen functional groups and hydrogen-terminated edge sites. Using this technique, we compared the total gas evolved for the two catalysts, revealing that MCP8-2000 evolved ∼3.5 times less total gas than MCP8, indicating that edge sites in MCP8-2000 are much lower, decreasing the susceptibility to corrosion (Table S3). The total gas evolved (reflecting total oxygen and H-terminated functional groups) from MCP8-2000 is similar to what has been reported for highly oriented pyrolytic graphite (HOPG), suggesting the presence of graphene sheets in the MCP8-2000 (as proven in Fig. 5d).[45]

Comparison of the overall stability of Pt/MCP8-2000 GDE *versus* commercial CCM. The performance and stability (10 000 voltage cycles between 0.6 V and 0.9 V, with holds of 3 s at each voltage) of Pt/MCP8-2000 GDEs with Pt mass loading of 0.3 mg cm^{-2} were measured. Furthermore, commercial carbon catalyst-coated membranes (Pt/C) with Pt mass loadings of 0.4 mg cm^{-2} were also tested for both carbon corrosion and Pt dissolution under identical conditions (Fig. 6). The BoL performance of the Pt/MCP8-2000 is as high as that of commercial catalyst-coated membranes (CCM), despite the lower Pt loading of the Pt/MCP8-2000 GDEs (see Fig. 6a and b). The Pt/MCP8-2000 showed 3–7 times lower potential losses (depending on the current density value) compared with

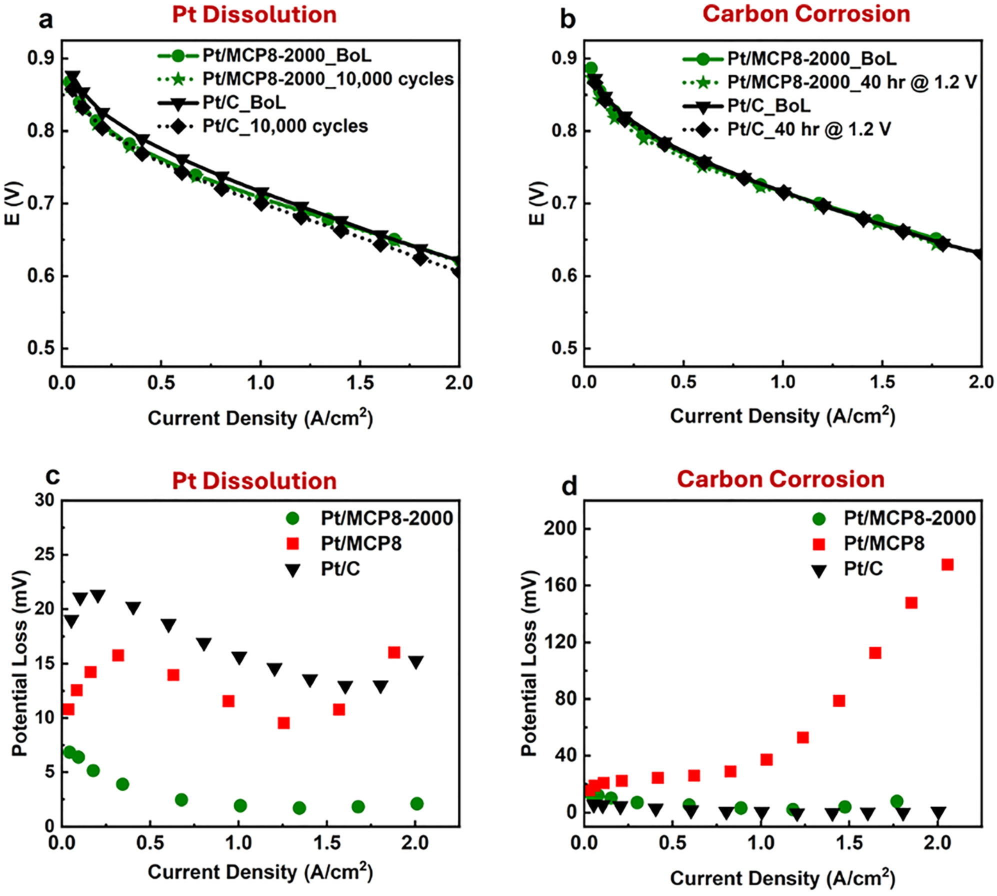

Fig. 6 Electrochemical performance of Pt/MCP8, Pt/MCP8-2000 (carbon post heat treated at 2000 °C)) catalyst layers and state-of-the-art commercial Pt/C powder catalyst layer in PEMFC MEAs. (a) H_2/air performance (non-IR-corrected) of MEAs of commercial Pt/C (catalyst coated membrane (CCM)) and Pt/MCP8-2000, (Pt mass loading in Pt/MCP8-2000= 0.27 mg_{Pt} cm^{-2}) at BoL and EoL (after10 000 AST square-wave cycles between 0.6 V and 0.95 V in 100% R.H., with 3 second holds at each potential) at 100% RH, 150 kPa_{abs}, and 80 °C. (b) H_2/air performance (non-IR-corrected) of MEAs of commercial Pt/C (carbon coated membrane (CCM)) and Pt/MCP8-2000, (Pt mass loading in Pt/MCP8-2000 = 0.29 mg_{Pt} cm^{-2}) at BoL and EoL (after holding the potential at 1.2 V for 40 h in H_2/Ar) at 100% RH, 150 kPa_{abs}, and 80 °C. (c) and (d) Potential losses as a function of MEAs of commercial Pt/C (carbon-coated membrane (CCM)), Pt/MCP8, and Pt/MCP8-2000 after 10 000 cycles of Pt dissolution (square-wave cycles between 0.6 V and 0.95 V in 100% R.H., with 3 second holds at each potential) and 40 h of carbon corrosion (holding potential at 1.2 V).

commercial CCM due to Pt dissolution after 10 000 cycles (see Fig. 6a–c). The commercial CCM and Pt/MCP8-2000 showed minimal performance loss after 40 hours at 1.2 V (carbon corrosion), while Pt/MCP8 exhibited significant performance loss due to carbon degradation, attributed to its less graphitic structure and higher density of defects and functional groups, which are more susceptible to degradation (see Fig. 6b). Among the three catalysts, MCP8-2000 offers minimal performance losses after Pt dissolution and carbon corrosion, compared with the Pt/MCP8 GDE and commercial CCM (see Fig. 6c and d). Most of the voltage loss in the Pt/MCP8-2000 CL is at low current density and might be attributed to agglomeration and a decrease in mass activity after 10 000 cycles of Pt dissolution (see Fig. 5c). TEM images were obtained to investigate the change in Pt NPs in Pt/MCP8-2000 after Pt dissolution (10 000 cycles) and carbon corrosion (40 hours at 1.2 V) tests. The TEM images show a 30% increase in particle size, with the average particle growing from 3.25 ± 0.81 nm to 4.26 ± 1.15 nm, as shown in Fig. S14. Moreover, the Pt particle size increases by the same percentage when carbon corrosion and Pt dissolution protocols are applied.

Pt/MCP8 GDE for heavy-duty applications. We further tested the stability of the Pt/MCP8-2000 GDE after 90 000 cycles of Pt dissolution, which the United States Department of Energy (DOE) requires for high-duty vehicle applications.[4] To complement the comparison with the commercial CCM shown in Fig. 6, Fig. 7a benchmarks the Pt/MCP8-2000 catalyst against representative Pt and Pt-alloy catalysts reported in the literature,[4] especially at low current density. For example, Liu *et al.*[20] reported minimal performance loss at 1.5 A cm^{-2} after 90 000 AST cycles due to Pt dissolution, their study does not address degradation from carbon corrosion—a key factor in catalyst layer stability and device lifetime. Additionally, their H_2/air performance (~1.8 A cm^{-2}@0.6 V) was achieved at 94 °C, 250 kPa_{abs}, and 100% RH. In contrast, our study achieved higher performance (~2.4 A cm^{-2}@0.6 V) at lower temperature (80 °C) and pressure (150 kPa_{abs}), demonstrating a rare combination of high performance, Pt dissolution resistance, and carbon corrosion durability in a purely Pt-based catalyst layer.

We investigated the change in the electrochemical surface area (ECSA) as a function of platinum (Pt) dissolution cycles (Fig. S15). After 90 000 cycles, the ECSA decreased by half. This decrease can be attributed to Pt nanoparticle (NP) agglomeration, with the size of Pt NPs increasing from 2.22 ± 0.66 nm to 4.93 ± 2.02 nm as shown in Fig. S16. The ECSA values exhibit a linear relationship with the number of cycles. This linear trend suggests that the degradation mechanisms remain consistent throughout the cycling process and that degradation likely occurs at a constant rate. Furthermore, it implies that catastrophic secondary mechanisms, such as carbon support collapse, may not be triggered under the given AST conditions, thereby avoiding accelerated degradation.

TEM images and EDS analysis of the cross-section of BoL and EoL Pt/MCP8-2000 GDEs reveal distinct changes, as shown in Fig. S17. At BoL, the cross-section shows a uniform distribution of Pt and Nafion (concentrated on the outside surface of the carbon agglomerate) across the thickness of the catalyst layer. After 90 000 cycles, the Pt band is observed near the membrane and cathode interface, revealing Pt dissolution and diffusion to the membrane (see Fig. S18), contributing to ECSA and the performance losses shown in Fig. 7a. However, no significant Pt agglomeration in the layer is observed, indicating that the performance degradation is mainly caused by the loss of Pt to the membrane. This indicates that the Pt/MCP8-2000 can withstand at least 90 000 cycles before noticeable effects occur. This stability could be for two reasons: (1) the pore confinement effect hinders the Pt agglomeration from the MCP8-2000, and (2) the carbon support itself after 2000 °C heat treatment becomes more graphitic with fewer defect sites (Fig. S13 and S19) and provides Pt with a robust environment that is less susceptible to corrosion.

Finally, we compared the key performance indicators (KPIs) of the Pt/MCP8-2000 GDE with the 2025 DOE targets for heavy-duty applications. MCP8-2000 GDE nearly meets, and even surpasses, some KPIs, such as the DOE targets in efficiency, power density, utilization, and lifetime (see Fig. 7b). The Pt mass loading used in Pt/MCP8-2000 GDE is 0.3 mg_{Pt} cm^{-2} (cathode), and that used in anodic coated membrane (ACM) is 0.1 mg_{Pt} cm^{-2} (anode), giving a total of 0.4 mg_{Pt} cm^{-2}.

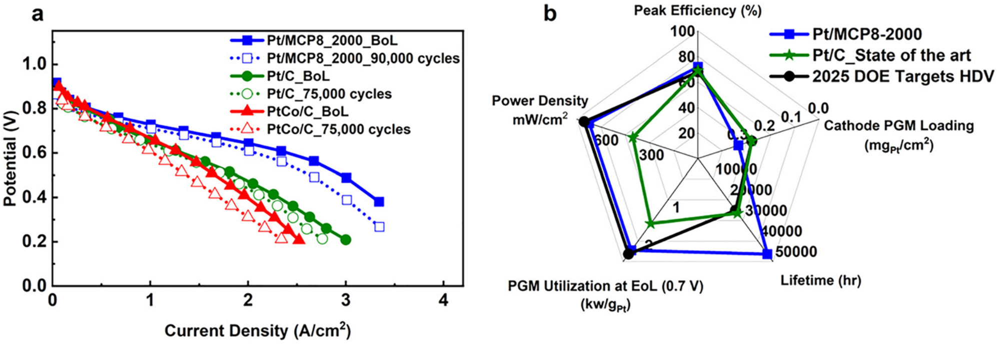

Fig. 7 A single PEMFC performance and key performance indicators (KPIs) comparison with previously reported studies and 2025 DOE targets. (a) H_2/air performance (non-IR-corrected) of MEAs of this work (Pt/MCP8-2000; Pt mass loading 0.3 mg_{Pt} cm^{-2}) and previously reported Pt/C and PtCo/C (Pt mass loading 0.25 mg_{Pt} cm^{-2})[47] at 100% RH, 150 kPa_{abs}, and 80 °C. (b) KPIs of this work compared to the 2025 DOE targets.

The target for the DOE is 0.3 mg_{Pt} cm^{-2} for both anode and cathode. We used a slightly higher loading (0.3 *vs.* 0.25 mg cm^{-2}) in the cathode, and used a high anode loading to eliminate any losses that might come from the anode side so that we could closely study the performance and the durability that results from the cathode side.

Conclusions

In this study, we demonstrate a significant advancement in PEMFC catalyst development by achieving simultaneous mitigation of Pt dissolution and carbon corrosion while maintaining high performance for heavy-duty applications. Mesoporous carbon powders with an 8 nm pore size (MCP8) were found to effectively reduce Pt dissolution and performance losses compared to 12 nm carbon (MCP12). We attribute this improvement to a pore confinement effect, as evidenced by experimental observations showing Pt nanoparticle growth occurring primarily in the interior of Pt/MCP12 agglomerates, compared to the growth exclusively on the outer surfaces of Pt/MCP8 agglomerates. To overcome MCP8's susceptibility to carbon corrosion, high-temperature treatment at 2000 °C under nitrogen was used to enhance its stability, enabling the catalyst layer to maintain its high performance after carbon corrosion accelerated stress tests. These heat-treated Pt/MCP8-2000 catalyst layers, fabricated as gas diffusion electrodes (GDEs), outperformed commercial catalyst-coated membranes (CCMs) in both stability and durability, retaining their high performance over 90 000 stress cycles. These results exceed the DOE 2025 targets, demonstrating the potential of Pt/MCP8-2000 GDEs to advance the commercialization of PEMFCs for heavy-duty applications. Finally, the effect of pore size and graphitization of the carbon support on mitigating Pt migration and dissolution can be explored in future studies using operando and *in situ* advanced X-ray synchrotron techniques, such as X-ray fluorescence and X-ray absorption spectroscopy.

Methods

Mesoporous carbon powder (MCP) preparation

3.0 g of mesophase pitch (MP, momentum Materials Solutions (https://momentummaterials.ca/mesophase-pitch)) and 9.0 grams of *n*-butanol (Sigma, >99%) were mixed in a 250 mL conical flask and stirred (*ca.* 600 rpm) at room temperature for three hours. Then, 7.5 g of 1,3 propanediol (PD, Aldrich, 98%) and 55.0 g of ultrapure water (8.2 mOhm.cm, total organic carbon [TOC] <5 ppb) are added to the MP mixture and sonicated for one hour and stirred (*ca.* 600 rpm) overnight. Finally, 60.0 g of a freshly prepared mixture of LUDOX SM colloidal silica (Aldrich, 30 wt%, for MCP8) or LUDOX HS-40 colloidal silica (Aldrich, 40 wt%, for MCP12) and 1,3 PD (14.0 g of 1,3 PD and 50.0 g of the colloidal silica) were added to the MP slurry. The mixture is then heated at around 60 °C until the complete evaporation of all solvents. The remaining solid mixture was collected, then ground, and finally carbonized at 900 °C. After carbonization, the powder collected was soaked in 1000 mL of 3 M NaOH in a Teflon bottle in the oven, at 80 °C to remove the templated silica. As a final step, the powder was soaked in water for one day at 80 °C and then collected by filtration. Following the filtration, the MCP powder was washed with water and then ethanol and finally collected and dried overnight in the oven at 80 °C. All MCP samples were heat-treated at 1500 °C for 2 hours under vacuum to reduce their hydrophilicity. The heating rate was controlled at 5 °C min^{-1}, followed by air cooling. All heat treatments were performed using a high-temperature furnace (model HP20-3560-20, Thermal Technology LLC). For MCP8-2000, the pristine MCP8 has been heat treated at 2000 °C for 2 hours under vacuum (ramping rate is 10 °C min^{-1}).

Gas diffusion electrode (GDE) fabrication and testing

Spraying carbon ink on GDE preparation. For gas diffusion electrodes (GDE) preparation, an ink of nanoporous carbon was sprayed first on the microporous layer (MPL) side, and then ALD of the catalyst was done on the carbon-loaded MPL/GDL (H23C8). The sprayed ink of the Ketjen Black (KB EC300J) and MCP carbons are made by mixing 60 mg of carbon with 15 mL of isopropyl alcohol. Every GDL was sprayed with approximately 2.5 mL of this ink formulation, giving a total Pt loading of approximately 0.1 mgC cm^{-2}. The temperature of the spraying plate was set at 120 °C with a flow rate of 100 μL min^{-1}.

Pt atomic layer deposition process (ALD). Trimethyl (methylcyclopentadienyl) platinum(IV) ($MeCpPtMe_3$, Strem Chemicals) was used as the Pt ALD precursor, and air was used as the oxidant. Pt ALD was conducted using the carbon-coated MPL/GDL as substrates at a reactor temperature of 190 °C, and the Pt precursor cylinder was heated to 78 °C. The exposure time to the Pt precursor and air was optimized at 8 s and 5 s, respectively, with a 0.2 s air dose being used. Argon was used as an inert gas to remove any excess reactant. The Ar purge time after Pt precursor exposure was 100 s, and the purge time after air exposure was 50 s.

Membrane electrode assembly (MEA) assembly and testing. MEAs were prepared by assembling 2–3 cm^2 of the fabricated GDE as cathodes with commercial anode-coated membranes. The ALD-prepared MEAs were conditioned and tested under differential flow at 80 °C, 100% relative humidity (RH), and 150 kPa back pressure.

To quantify the electrochemical surface area (ECSA), a cyclic voltammogram (CV) between 0.06 and 0.6 V (50 mV s^{-1}) was measured after purging the cathode with Ar. The average current in the capacitive region provided the parasitic H_2 crossover current used for background correction. All subsequent electrochemical measurements were carried out at 80 °C, 100% R.H., and 1.5 bar absolute pressure.

Air–H_2 polarization curves were measured in 5000 sccm house air with 3 min current holds (U.S. DOE protocol). Throughout the entire testing sequence, 500 sccm H_2 (99.999%, Praxair) was flown through the anode at 100% relative humidity. To break in the MEA, a cathode recovery protocol was performed by maintaining a 0.1 V bias for 4 h in air (1000 sccm) at 40 °C and 150% relative humidity (RH).[48]

The accelerated stress test (square-wave cycles between 0.6 V and 0.95 V with 3 s holds at each potential), was carried out in 1000 sccm H_2 and 5000 sccm Ar at 80 °C, 100% RH, and 150 kPa absolute backpressure. For support stability, the cell was held at 1.2 V for 40 hours in H_2/Ar at 80 °C and 100% RH. The gas flow was kept at 1000 sccm at anode and cathode and 1.5 bar absolute back pressure.

We estimated the fuel cell lifetime following the study by Peng *et al.*[49] The department of energy (DOE) defines fuel cell lifetime as the operational duration until a 10% reduction in cell voltage at the rated power is observed. To analyze voltage loss, we selected a current density of 1.5 A cm^{-2}, corresponding to the current density at which the targeted rated power is delivered at a rated voltage of 0.67 V. The lifetime of the tested MEA is estimated using the ratio of 10% of the initial voltage (V_{initial}) at 1.5 A cm^{-2} to the voltage loss rate at the same current density, as expressed in the equation below.[49] An acceleration factor of 100 (in terms of time) relative to the drive cycle is applied, consistent with prior studies.[50] Each complete square-wave cycle spans 6 seconds (3 seconds at 0.60 V and 3 seconds at 0.95 V)

$$\text{Lifetime (h)} = \frac{10\% \times V_{\text{initial}}(\text{mV})}{\text{voltage loss rate}\left(\dfrac{\text{mv}}{\text{cycle}}\right)} \times 6\left(\frac{\text{s}}{\text{cycle}}\right) \times \frac{100}{3600}\left(\frac{\text{s}}{\text{h}}\right)$$

Physical characterization

An AMETEK Spectro Xepos HE X-ray fluorescence (XRF) Spectrometer was used to estimate the Pt loading of all ALD-Pt/C films. The GDE is placed in the center of the XRF holder. Helium gas was used as a carrier gas at a flow rate of 85 ± 2 μL min^{-1}.

High-temperature programmed desorption (TPD) was performed using an in-house high vacuum apparatus, allowing quantitative detection of gases evolved during the heating of samples to 1800 °C at 10 °C min^{-1}. At these high temperatures, most of the carbon edge sites terminated by H or O were decomposed, forming H_2, H_2O, CO, and CO_2, thus allowing the number of edge sites to be estimated.

X-ray photoelectron spectroscopy (XPS) was conducted using the PHI Versaprobe 4 at Stanford nano shared facility (SNSF) with Al Kα radiation. The PHI instrument-specific relativity sensitivity factors were used and all XPS spectra were obtained from the bare surfaces, without the use of monoatomic argon sputtering. In addition, all XPS spectrums were calibrated employing the adventitious carbon peak at 248.8 eV.

For nitrogen gas sorption, a 3Flex Version 3.01 gas sorption instrument (Canadian foundation for innovation (CFI)) was used to run nitrogen gas sorption analysis and determine the specific surface area and porosity of the carbon samples. 100 mg of carbon powders were used in each measurement. Data were collected at 77 K with prior degassing in N_2 at 150 °C for 4 h and then degassing at a pressure lower than 10–3 Torr before the measurements. The specific surface area of the MCP in $m^2\ g^{-1}$ was obtained using the Brunauer–Emmett–Teller (BET) plot in the range of $0.05 < P/P_0 < 0.3$, where P is the N_2 partial pressure and P_0 is the N_2 vapor pressure. The total pore volume was calculated at $P/P_0 = 0.98$, and the pore size distributions were obtained from the adsorption and desorption branches, measured using the Barrett–Joyner–Halenda (BJH) method with Faas correction based on Carbon Black materials.

Transmission electron microscope (TEM) samples were prepared as follows: CCM samples, a 0.5 cm × 0.5 cm portion of the CCMs was cut with scissors Then, the GDL was carefully removed from each MEA using tweezers. A small section of each CCM was embedded in a mixture of resin and hardener in equal parts (obtained from Sigma-Aldrich, USA) and left to solidify overnight, allowing the sample to be prepared for ultramicrotomy. Thin 100 nm sections were sliced using a Leica UCT ultramicrotome setup (Germany) equipped with an Ultra 45°DiATOME knife (USA). These sections were then mounted on multiple 200 mesh Cu/Pd grids.

For imaging of the samples, a Talos F200X STEM (Thermo Fisher Scientific, USA) with a 200 kV electron accelerating voltage and super-X four silicon drift detectors of energy dispersive X-ray spectrometry (Super-X SDD EDXS, Bruker, USA) was utilized. To analyze the catalyst particles, TEM images were captured at 190 k× using the bright field detector. Fiji ImageJ software was used to extract the particle size distribution (PSD), measuring a minimum of 200 platinum particles. EDS maps were obtained on at least 5 different randomly selected regions. STEM-EDS maps of the catalyst layers were collected at 5 k× and 79 k× magnification. The EDS maps were acquired with an electron dose of 2.34×10^4 e-nm^{-2} and processed using ESPIRIT 1.9 (Bruker, USA) software.

Author contributions

Conceptualization: M. A., F. B. P., S. X. Methodology: M. A., S. P. S. X., S. D., J. J., F. B. P. Investigation: M. A., S. P., S. X., S. D., Y. J., T. Y., R. S., R. X., R. M., H. N., J. J., Y. C. T. F. J., F. B. P. Writing – original draft: M. A. Writing – review & editing: M. A., S. P., S. X., S. D., Y. J., T. Y., R. S., R. X., R. M., H. N., J. J., Y. C. T. F. J., F. B. P. Visualization: M. A. Supervision: J. J. R. M., H. N., Y. C., T. F. J., F. B. P. Funding acquisition: T. F. J., F. B. P.

Conflicts of interest

The authors declare no competing interests.

Data availability

All raw data supporting the findings of this study, including electrochemical performance, SEM, TEM, XRD, EDS, and other experimental analyses presented in the manuscript, are available.

Supplementary information (SI) is available. See DOI: https://doi.org/10.1039/d6ey00019c.

Acknowledgements

This work was supported financially by the Volkswagen Group of America through contract 1239072-1-UBMSI. Part of the work was performed at the Stanford Nano Shared Facilities (SNSF), supported by the National Science Foundation under award ECCS-2026822. This work was partly supported by JST PRESTO grant no. JPMJPR23QA, helped in TPD measurement and 2000 °C treatment.

References

1 M. K. Debe, *Nature*, 2012, **486**, 43–51.
2 V. R. Stamenkovic, D. Strmcnik, P. P. Lopes and N. M. Markovic, *Nat. Mater.*, 2016, **16**, 57–69.
3 D. Banham and S. Ye, *ACS Energy Lett.*, 2017, **2**, 629–638.
4 D. A. Cullen, K. C. Neyerlin, R. K. Ahluwalia, R. Mukundan, K. L. More, R. L. Borup, A. Z. Weber, D. J. Myers and A. Kusoglu, *Nat. Energy*, 2021, **6**, 462–474.
5 E. Colombo, A. Baricci, A. Bisello, L. Guetaz and A. Casalegno, *J. Power Sources*, 2023, **553**, 232246.
6 P. C. Okonkwo, I. Ben Belgacem, W. Emori and P. C. Uzoma, *Int. J. Hydrogen Energy*, 2021, **46**, 27956–27973.
7 E. Colombo, A. Baricci, D. Mora, L. Guetaz and A. Casalegno, *J. Power Sources*, 2023, **580**, 233376.
8 C. L. Yang, L. N. Wang, P. Yin, J. Liu, M. X. Chen, Q. Q. Yan, Z. S. Wang, S. L. Xu, S. Q. Chu, C. Cui, H. Ju, J. Zhu, Y. Lin, J. Shui and H. W. Liang, *Science*, 2021, **374**, 459–464.
9 C. Lee, S. Komini Babu, B. M. Patterson, K. S. Reeves, H. Yu, D. A. Cullen, R. Mukundan, R. L. Borup and J. S. Spendelow, *J. Electrochem. Soc.*, 2024, **171**, 014502.
10 P. C. Okonkwo, O. O. Ige, E. M. Barhoumi, P. C. Uzoma, W. Emori, A. Benamor and A. M. Abdullah, *Int. J. Hydrogen Energy*, 2021, **46**, 15850–15865.
11 Z. W. Seh, J. Kibsgaard, C. F. Dickens, I. Chorkendorff, J. K. Norskov and T. F. Jaramillo, *Science*, 2017, **355**, eaad4998.
12 L. Castanheira, W. O. Silva, F. H. B. Lima, A. Crisci, L. Dubau and F. Maillard, *ACS Catal.*, 2015, **5**, 2184–2194.
13 S. Xu, Z. Wang, S. Dull, Y. Liu, D. U. Lee, J. S. Lezama Pacheco, M. Orazov, P. E. Vullum, A. L. Dadlani, O. Vinogradova, P. Schindler, Q. Tam, T. D. Schladt, J. E. Mueller, S. Kirsch, G. Huebner, D. Higgins, J. Torgersen, V. Viswanathan, T. F. Jaramillo and F. B. Prinz, *Adv. Mater.*, 2021, **33**, e2007885.
14 B. Liu, R. Feng, M. Busch, S. Wang, H. Wu, P. Liu, J. Gu, A. Bahadoran, D. Matsumura, T. Tsuji, D. Zhang, F. Song and Q. Liu, *ACS Nano*, 2022, **16**, 14121–14133.
15 A. Sivanantham, P. Ganesan, L. Estevez, B. P. McGrail, R. K. Motkuri and S. Shanmugam, *Adv. Energy Mater.*, 2018, **8**, 1702838.
16 J. Hou, Y. Wu, S. Cao, Y. Sun and L. Sun, *Small*, 2017, **13**, 1702018.
17 Y. Chen, J. Pei, Z. Chen, A. Li, S. Ji, H. Rong, Q. Xu, T. Wang, A. Zhang, H. Tang, J. Zhu, X. Han, Z. Zhuang, G. Zhou and D. Wang, *Nano Lett.*, 2022, **22**, 7563–7571.
18 W.-J. Lee, S. Bera, H. Woo, H. G. Kim, J.-H. Baek, W. Hong, J.-Y. Park, S.-J. Oh and S.-H. Kwon, *Chem. Mater.*, 2022, **34**, 5949–5959.
19 Z. Song, B. Wang, N. Cheng, L. Yang, D. Banham, R. Li, S. Ye and X. Sun, *J. Mater. Chem. A*, 2017, **5**, 9760–9767.
20 Z. Liu, B. Peng, Y. J. Tsai, A. Zhang, M. Xu, W. Zang, X. Yan, L. Xing, X. Pan, X. Duan and Y. Huang, *Nat. Nanotechnol.*, 2025, **20**, 807–814.
21 L. Strandberg, V. Shokhen, M. Skoglundh and B. Wickman, *ACS Catal.*, 2024, **14**, 8494–8504.
22 E. Yli-Rantala, A. Pasanen, P. Kauranen, V. Ruiz, M. Borghei, E. Kauppinen, A. Oyarce, G. Lindbergh, C. Lagergren, M. Darab, S. Sunde, M. Thomassen, S. Ma-Andersen and E. Skou, *Fuel Cells*, 2011, **11**, 715–725.
23 H. Schmies, E. Hornberger, B. Anke, T. Jurzinsky, H. N. Nong, F. Dionigi, S. Kühl, J. Drnec, M. Lerch, C. Cremers and P. Strasser, *Chem. Mater.*, 2018, **30**, 7287–7295.
24 Z. Zhao, Z. Liu, A. Zhang, X. Yan, W. Xue, B. Peng, H. L. Xin, X. Pan, X. Duan and Y. Huang, *Nat. Nanotechnol.*, 2022, **17**, 968–975.
25 J. Knossalla, P. Paciok, D. Gohl, D. Jalalpoor, E. Pizzutilo, A. M. Mingers, M. Heggen, R. E. Dunin-Borkowski, K. J. J. Mayrhofer, F. Schuth and M. Ledendecker, *J. Am. Chem. Soc.*, 2018, **140**, 15684–15689.
26 B. Yang, C. Hao, Q. Liao, J. Liu, B. Yan, M. Lin, P. K. Shen, L. Feng and Z. Q. Tian, *J. Colloid Interface Sci.*, 2025, **683**, 460–473.
27 J. W. Shim, J. Koo, S. J. Yoo and J. H. Shim, *ACS Sustainable Chem. Eng.*, 2024, **12**, 15634–15642.
28 H. W. Park, B. G. Seo, J. W. Shim, N. Il Kim, Y. S. Choi and J. H. Shim, *Appl. Catal., B*, 2023, **337**, 122956.
29 M. Atwa, X. Li, Z. Wang, S. Dull, S. Xu, X. Tong, R. Tang, H. Nishihara, F. Prinz and V. Birss, *Mater. Horiz.*, 2021, **8**, 2451–2462.
30 M. Atwa, S. Xu, X. Li, S. Dull, Z. Wang, H. Yu, R. Tang, T. Goh, Y. Jung, M. Kiani, M. Lid, H. Nishihara, F. B. Prinz and V. Birss, *J. Mater. Chem. A*, 2025, **13**, 33587–33600.
31 L. J. A. E. S. Kovats, *Langmuir*, 1994, **10**, 4225–4231.
32 M. Thommes, K. Kaneko, A. V. Neimark, J. P. Olivier, F. Rodriguez-Reinoso, J. Rouquerol and K. S. W. Sing, *Pure Appl. Chem.*, 2015, **87**, 1051–1069.
33 E. P. Barrett, L. G. Joyner and P. P. Halenda, *J. Am. Chem. Soc.*, 1951, **73**, 373–380.
34 B. C. Lippens and J. H. De Boer, *J. Catal.*, 1965, **4**, 319–323.
35 V. Yarlagadda, M. K. Carpenter, T. E. Moylan, R. S. Kukreja, R. Koestner, W. Gu, L. Thompson and A. Kongkanand, *ACS Energy Lett.*, 2018, **3**, 618–621.
36 V. Yarlagadda, N. Ramaswamy, R. S. Kukreja and S. Kumaraguru, *J. Power Sources*, 2022, **532**, 231349.
37 M. Ko, E. Padgett, V. Yarlagadda, A. Kongkanand and D. A. Muller, *J. Electrochem. Soc.*, 2021, **168**, 024512.
38 S. M. Dull, S. Xu, T. Goh, D. U. Lee, D. Higgins, M. Orazov, D. M. Koshy, P. E. Vullum, S. Kirsch, G. Huebner, J. Torgersen, T. F. Jaramillo and F. B. Prinz, *Cell Rep. Phys. Sci.*, 2021, **2**, 100297.
39 W. Wang, K. Li, L. Ding, S. Yu, Z. Xie, D. A. Cullen, H. Yu, G. Bender, Z. Kang, J. A. Wrubel, Z. Ma, C. B. Capuano,

A. Keane, K. Ayers and F. Y. Zhang, *ACS Appl. Mater. Interfaces*, 2022, **14**, 9002–9012.

40 A. Kobayashi, T. Fujii, C. Harada, E. Yasumoto, K. Takeda, K. Kakinuma and M. Uchida, *ACS Appl. Energy Mater.*, 2021, **4**, 2307–2317.

41 B. S. Kim, J. H. Park and J. S. Park, *Membranes*, 2023, **13**, 794–810.

42 S. Ott, A. Orfanidi, H. Schmies, B. Anke, H. N. Nong, J. Hübner, U. Gernert, M. Gliech, M. Lerch and P. Strasser, *Nat. Mater.*, 2020, **19**, 77–85.

43 C. Galeano, J. C. Meier, V. Peinecke, H. Bongard, I. Katsounaros, A. A. Topalov, A. Lu, K. J. Mayrhofer and F. Schuth, *J. Am. Chem. Soc.*, 2012, **134**, 20457–20465.

44 O. V. Kharissova and B. I. Kharisov, *RSC Adv.*, 2014, **4**, 30807–30815.

45 H. Nishihara, T. Simura, S. Kobayashi, K. Nomura, R. Berenguer, M. Ito, M. Uchimura, H. Iden, K. Arihara, A. Ohma, Y. Hayasaka and T. Kyotani, *Adv. Funct. Mater.*, 2016, **26**, 6418–6427.

46 R. Tang, K. Taguchi, H. Nishihara, T. Ishii, E. Morallón, D. Cazorla-Amorós, T. Asada, N. Kobayashi, Y. Muramatsu and T. Kyotani, *J. Mater. Chem. A*, 2019, **7**, 7480–7488.

47 R. L. W. Borup and A. Z. Fc-pad, *Fuel Cell Performance and Durability Consortium*, 2020.

48 S. M. Dull, O. Vinogradova, S. Xu, D. M. Koshy, P. E. Vullum, J. Torgersen, S. Kirsch, V. Viswanathan, T. F. Jaramillo and F. B. Prinz, *ACS Appl. Energy Mater.*, 2022, **5**, 8282–8291.

49 Z. L. Bosi Peng, L. Sementa, Q. Jia, Q. Sun, E. L. Carlo, U. Segre, M. Xu, Y.-H. (Joseph) Tsai, X. Yan, Z. Zhao, J. Huang, X. Pan, X. Duan and Y. H. Alessandro Fortunelli, *Nat. Catal.*, 2024, **7**, 818–828.

50 S. Stariha, N. Macauley, B. T. Sneed, D. Langlois, K. L. More, R. Mukundan and R. L. Borup, *J. Electrochem. Soc.*, 2018, **165**, F492–F501.